



HAL
open science

Equilibrium mass-dependent isotope fractionation of antimony between stibnite and Sb secondary minerals: A first-principles study

Colin Ferrari, Merlin Méheut, Eléonore Resongles, Rémi Freydier, Corinne Casiot

► **To cite this version:**

Colin Ferrari, Merlin Méheut, Eléonore Resongles, Rémi Freydier, Corinne Casiot. Equilibrium mass-dependent isotope fractionation of antimony between stibnite and Sb secondary minerals: A first-principles study. *Chemical Geology*, 2022, 611, pp.121115. 10.1016/j.chemgeo.2022.121115. hal-03812631

HAL Id: hal-03812631

<https://hal.science/hal-03812631>

Submitted on 12 Oct 2022

HAL is a multi-disciplinary open access archive for the deposit and dissemination of scientific research documents, whether they are published or not. The documents may come from teaching and research institutions in France or abroad, or from public or private research centers.

L'archive ouverte pluridisciplinaire **HAL**, est destinée au dépôt et à la diffusion de documents scientifiques de niveau recherche, publiés ou non, émanant des établissements d'enseignement et de recherche français ou étrangers, des laboratoires publics ou privés.

Equilibrium antimony mass-dependent isotope fractionation between stibnite and Sb secondary minerals: a first-principles study

1 Colin Ferrari ^{*a}, Merlin Méheut ^b, Eléonore Resongles ^a, Rémi Freyrier ^a and Corinne Casiot ^a

2 ^a*HydroSciences Montpellier, Univ. Montpellier, CNRS, IRD, Montpellier, France*

3 ^b*Géosciences Environnement Toulouse, CNRS-UPS-OMP, 14 av. Edouard Belin, 31400 Toulouse, France*

4 *Corresponding author

5 Mailing address : Université de Montpellier – CC 57

6 163, rue Auguste Broussonnet,

7 34090 Montpellier, France

8 Email : colin.ferrari@umontpellier.fr

9 Abstract

10 Antimony (Sb) isotopes are gaining increasing interest for their potential as geochemical tracers in geological,
11 environmental and archaeological studies. However, little is known about the parameters controlling Sb
12 isotope fractionation, which is essential to interpret variations of isotopic signature in natural systems. In this
13 study, equilibrium mass-dependent isotope fractionation factors (β -factor) were determined between different
14 Sb-bearing minerals commonly found in mining environments including primary Sb sulphide (stibnite Sb_2S_3) and
15 its oxidation products (valentinite Sb_2O_3 , senarmontite Sb_2O_3 , cervantite Sb_2O_4) and synthetic antimony
16 pentoxide Sb_2O_5 . First-principles calculations within the Density Functional Theory (DFT) were performed with
17 different functionals to test the robustness of the method. Among the studied minerals, stibnite has the lowest
18 β -factor ($\ln(\beta) = 0.71 \text{ ‰}$ at 22°C), then β -factors progressively increase from valentinite ($\ln(\beta) = 1.64 \text{ ‰}$ at
19 22°C), to senarmontite ($\ln(\beta) = 1.80 \text{ ‰}$ at 22°C), cervantite ($\ln(\beta) = 2.20 \text{ ‰}$ at 22°C) and antimony pentoxide
20 ($\ln(\beta) = 3.03 \text{ ‰}$ at 22°C). The parameters that most fractionate Sb isotopes are found to be i) the change of Sb
21 oxidation state (Sb isotope ratio in Sb(V)-bearing minerals is higher than in Sb(III)-bearing minerals), ii) the
22 change of first neighbour of Sb (Sb isotope ratio in Sb – O bonds is higher than in Sb – S bonds) and iii)
23 distortion of the atomic Sb - O polyhedrons. The negligible differences in the β -factors obtained with different
24 functionals showed the robustness of the approach for the calculation of β -factors, despite differences in the
25 calculated mineral lattice and Raman frequencies. The results of this study provide a theoretical basis to
26 interpret natural Sb isotope variations. In sulphide mining environments, the results suggest that a significant
27 enrichment in the heavy isotope could occur during oxidative dissolution of stibnite and subsequent
28 precipitation of Sb(III) and Sb(V) oxides. More generally, this work strongly supports that Sb isotopes may be a
29 useful tracer of Sb transformation processes in nature.

30 Keywords: Antimony, Equilibrium isotope fractionation, Density Functional Theory (DFT), Sb minerals, Ab initio
31 calculations.

321. Introduction

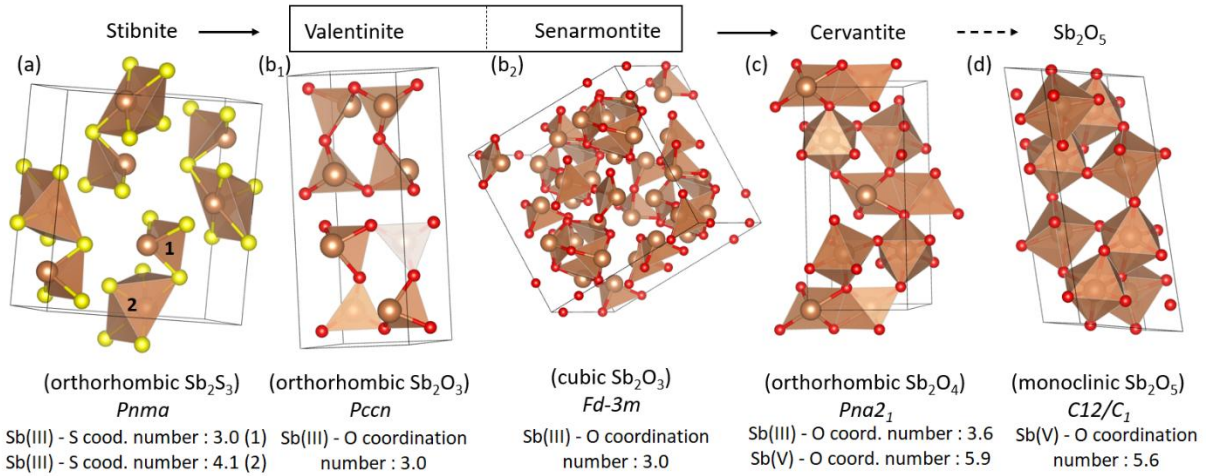
33 Antimony (Sb) is toxic for organisms and considered as a possible human carcinogen (Sundar and Chakravarty, 2010).
34 Global anthropogenic Sb emissions have dramatically increased during the 20th century and a further two-fold
35 increase is expected between 2010 and 2050 (Zhou et al., 2015). Anthropogenic sources of antimony emission
36 include mining and metallurgical industries, coal and fuel combustion, waste incineration and road traffic (He et al.,
37 2019; Tian et al., 2014). As a result, environmental contamination with Sb has been reported in various urban,

38 industrial and mining contexts (He et al., 2019). In particular, the mining of Sb- or base metals-sulphide ores is a
39 major cause of high environmental Sb concentrations (Hiller et al., 2012; Liu et al., 2010). However, compared to
40 other toxic metal(loid)s, the behaviour of Sb in the environment is poorly known.

41 Metal(loid) stable isotopes are useful geochemical tracers for tracking the sources and fate of metals in the
42 environment (Wiederhold, 2015). While some isotopic systems are relatively well-known (e.g. Cu, Zn (Moynier et al.,
43 2017)), only few studies have focused on antimony stable isotopes (^{121}Sb (57.21%) and ^{123}Sb (42.79%), Chang et al.,
44 1993). Rouxel et al. (2003) first showed that natural variations of the isotopic composition ($\delta^{123}\text{Sb}$) were wide
45 enough to be applied as a geochemical tracer and the potential of Sb isotopes as archaeological and environmental
46 tracers has been confirmed afterwards (Degryse et al., 2020, 2015; Dillis et al., 2019; Lobo et al., 2014, 2013;
47 Resongles et al., 2015). As for other stable isotope systems, Sb isotopes may be fractionated during (bio-
48)geochemical processes controlling Sb fate in surface environments (e.g. change of redox state, adsorption,
49 precipitation...) (Wiederhold, 2015). Documenting the direction and intensity of Sb isotope fractionation during
50 these processes is of primary importance to interpret Sb isotope signatures in complex environmental systems
51 (Komárek et al., 2021).

52 Metal isotope fractionation factors have been acquired from field observations, laboratory experimentations, or
53 theoretical calculations (Fujii et al., 2014; Schauble et al., 2009; Sherman, 2013; Wiederhold, 2015) but
54 investigations of Sb isotope fractionation are scarce. Rouxel et al. (2003) showed a large fractionation of Sb isotopes
55 during the abiotic reduction of aqueous Sb(V) to Sb(III). A recent experimental study showed no significant
56 equilibrium isotope fractionation due to adsorption of Sb on aluminium oxides while a kinetic fractionation was
57 observed in the first stage of the reaction (Zhou et al., 2022). Wang et al. (2021) and Zhai et al. (2021) showed large
58 $\delta^{123}\text{Sb}$ range of 0.75 ‰ and 1.13 ‰, respectively, among stibnite ores or Sb sulfosalts in the epithermal system but
59 the origin of Sb isotope fractionation during the precipitation of Sb-bearing mineral from the hydrothermal fluid is
60 still under debate (Wang et al., 2021; Zhai et al., 2021). To date, no theoretical study has been made to predict the
61 cause of Sb isotopic fractionation at equilibrium among various Sb minerals and different bonding environments,
62 and the current knowledge of Sb isotope fractionation caused by physical and biogeochemical processes is very
63 limited.

64 This study aims to determine mass dependant equilibrium isotopic fractionation factors between various Sb
65 minerals to provide a theoretical basis for the interpretation of Sb isotopic signatures in natural systems. For this, Sb
66 isotopic partitions at equilibrium were calculated between stibnite (Sb_2S_3), the main Sb primary ore and selected Sb
67 secondary minerals (senarmontite, valentinite, cervantite (Figure 1)) (Roper et al., 2012). The methodology is based
68 on the Density Functional Theory (DFT); it involves determining theoretically the vibrational properties of these
69 structures. The theoretical and quantum approach of DFT aims at estimating the relationship between fractionation
70 properties and interatomic bond strengths (Sb-S bond or Sb-O bond), or Sb redox change. In this work, we modelled
71 the oxidation steps of stibnite (orthorhombic $\text{Sb(III)}_2\text{S}_3$) towards a fully oxidized and synthetic Sb_2O_3 phase, via
72 valentinite (orthorhombic $\text{Sb(III)}_2\text{O}_3$), senarmontite (cubic $\text{Sb(III)}_2\text{O}_3$) and cervantite (orthorhombic $\alpha\text{-Sb(V)Sb(III)O}_4$)
73 by calculating their isotopic partition ^{123}Sb β -factor. To quantify the extent of Sb isotopic fractionation associated
74 with the different parameters controlling the isotopic fractionation, each site of cervantite has then been studied
75 and calculated separately to observe the effect of trivalent/pentavalent antimony and its oxygen bonds on the β -
76 factor. The site-by-site calculation have also been made with the two Sb sites in stibnite, where their coordination
77 number and average bond length are significantly different. This oxidation process, described by Roper et al. (2012),
78 commonly occurs in sulphide mining environments and plays an important role in Sb attenuation in the supergene
79 environments (Ashley et al., 2003; Filella et al., 2009). Computations have been made using two different
80 functionals (Local Density Approximation (LDA) and Generalized Gradient Approximation (GGA)). At all steps of the
81 calculation (relaxation, phonon dispersion; Infra-Red (IR) and Raman spectrum), results have been compared with
82 experimental values, when available (Cody et al., 1979; Mestl et al., 1994.; Sereni et al., 2010). The results are
83 expected to provide information on the direction and magnitude of Sb isotope fractionation factors, to help
84 interpretation of future field or experimental observations.



85

86 *Figure 1: Scheme of stibnite transformation process from Sb_2S_3 to Sb_2O_5 modelled in this study indicating the crystal system,*
 87 *the spacegroup of the minerals and Sb coordination number. The atomic structures were drawn with VESTA software as well*
 88 *as the coordination number determination (Momma et al., (2011)).*

89

90. Method

91

2.1 β -factors

92 The equilibrium isotope fractionation factor α_{B-A} between two mineral phases A and B corresponds to the ratio of Sb
 93 isotope ratios in these minerals and can be expressed as:

94

$$\alpha_{B-A} = \frac{\left(\frac{^{123}Sb}{^{121}Sb}\right)_B}{\left(\frac{^{123}Sb}{^{121}Sb}\right)_A} = \frac{\beta_B}{\beta_A} \quad (1)$$

95 Where β_x is the isotopic partition factor of a mineral X relative to an ideal atomic gas. As α is very close to 1, the
 96 isotopic fractionation factor can be expressed as (Schauble et al., 2009; Sherman, 2013):

97

$$1000 \ln \alpha_{B-A} = 1000(\ln \beta_B - \ln \beta_A) \approx \delta^{123}Sb_B - \delta^{123}Sb_A \quad (2)$$

98

$$\text{With } \delta^{123}Sb = \frac{(^{123}Sb/^{121}Sb)_{\text{sample}}}{(^{123}Sb/^{121}Sb)_{\text{standard}}} - 1 \quad (3)$$

99 Equilibrium mass-dependent isotope fractionation results from the effect of atomic mass on bond energy
 100 (Bigeleisen and Mayer, 1947; Urey, 1947). If A is a crystalline solid, and Y the element of interest, The β -factor of
 101 phase A for the Y/Y* substitution can be written as:

$$\beta(A Y_n, Y) = \left[\frac{Q(A Y_n^*)}{Q(A Y_n)} \right]^{\frac{1}{n}} \left[\frac{m_Y}{m_{Y^*}} \right]^{\frac{3}{2}} \quad (4)$$

102 where Y* the heavier isotope and Y the main isotope, m_Y and m_{Y^*} the respective mass of the isotopes Y and Y* and n
 103 the total number of sites. $Q(A Y_n^*)$ denotes the partition function of the system having all the Y isotopes substituted
 104 with Y* (Méheut-Le Quéau, 2008).

105 When the crystal structure presents two types of sites with significantly different environments, such as the Sb(III)
 106 and Sb(V) sites in cervantite, it is interesting to consider the local β -factor, relative to one type of site only. In this
 107 case, if the system is written $A Y_{1,i} Y_{2,j}$, with i and j the number of sites 1 and 2, the β -factor of site 1 is:

$$\beta(A_{Y_1}, Y) = \left[\frac{Q(A_{Y_{1,i}}^* Y_{2,j})}{Q(A_{Y_{1,i}} Y_{2,j})} \right]^{\frac{1}{T}} \left[\frac{m_Y}{m_{Y^*}} \right]^{\frac{3}{2}} \quad (5)$$

108 The partition function Q can then be computed from the vibrational properties of the system:

$$Q = \left[\prod_{i=1}^{3N^{at}} \prod_{\{q\}} \frac{\exp\left(-\frac{h\nu_{q,i}}{2kt}\right)}{1 - \exp\left(-\frac{h\nu_{q,i}}{kt}\right)} \right]^{\frac{1}{N_q}} \quad (6)$$

109 Where $\nu_{q,i}$ are the frequencies of the phonon with the wavevector \mathbf{q} and branch index $i=1, 2, 3$. N^{at} is the number of
 110 atoms in the unit cell, N is the number of sites for the Y atom in the unit cell, T is the temperature (K), k is the
 111 Boltzmann constant and h is Planck's constant. In the product of Eq. (6) the three translational $\mathbf{q}=0$ modes with
 112 $\nu_{q,i} = 0$ are not considered.

113 2.2 Computational methods

114 In this paper, electronic and vibrational properties are calculated within the first-principles plane waves method
 115 based on DFT through the Quantum espresso suite (version 6.4 (Giannozzi et al., 2017, 2009)). The starting
 116 structures are those experimentally determined for stibnite in orthorhombic $Pnma$ symmetry (Kyono and Kimata,
 117 2004), senarmontite in cubic $Fd-3m$ symmetry (Whitten et al., 2004), valentinite in $Pccn$ symmetry (Whitten et al.,
 118 2004), cervantite in $Pna2_1$ symmetry (Gopalakrishnan et al., 1975) and Sb_2O_5 in monoclinic $C12/c1$ symmetry (Jansen,
 119 1979). For stibnite, valentinite and cervantite, we use several functionals, namely the local approximation of Perdew
 120 and Zunger (PZ) (Perdew and Zunger, 1981), the generalized-gradient approximations to the exchange-correlation
 121 functional of Perdew, Burke and Ernzerhoff (PBE) (Perdew et al., 1996) and the recent PBEsol functional (Perdew et
 122 al., 2008). Previous models have shown good results for stibnite using the PZ (Filip et al., 2013) and PBESOL (Ibáñez
 123 et al., 2016) pseudopotentials. However, no model tested the PBE functional, it is then interesting to compare the
 124 results on these three different functionals. For senarmontite and Sb_2O_5 , only the PBEsol functional is used as it
 125 appears to be the most reliable. Ionic cores of each atom are described by either ultrasoft (us) or norm conserving
 126 pseudopotentials (nc). The pseudopotential for O is nc and is generated for PZ, PBE, or PBEsol with the same
 127 characteristics as described in the electronic annexes of Méheut et al. (2007). For S, the pseudopotential is from the
 128 PSLibrary (Dal Corso, 2014). For Sb, two types of pseudopotentials from the PSLibrary are considered: the "ultrasoft"
 129 (e.g. pseudopotential file `Sb.pz-dn-rrkjus_psl.1.0.0.UPF` for PZ functional) and the "norm-conserving" (e.g. `Sb-pz-n-`
 130 `nc.UPF` for PZ functional). The first one is in principle very accurate (due to the account of semicore states). This
 131 permits an accurate calculation at a reasonable computational cost, due to the ultrasoft approach. However, the
 132 computation of Raman intensities is not implemented for this type of pseudopotentials in the Quantum Espresso
 133 software package. In order to compute Raman intensities and compare more precisely calculated gamma-point
 134 frequencies with experiment, nc pseudopotentials only should be used. Calculations using the us or nc
 135 pseudopotentials for Sb will be thereafter called us or nc, respectively. For both types of calculations, electronic
 136 wave-functions are expanded in plane-waves up to an energy cutoff $\epsilon_{cut}=80$ Ry (1088 eV) and the charge density cut-
 137 off is set to $4 \epsilon_{cut}$. Electronic integration is done by sampling the Brillouin zone with a $4 \times 2 \times 4$ k-point grid for
 138 valentinite, a $2 \times 6 \times 2$ grid for stibnite, a $3 \times 4 \times 2$ grid for cervantite, a $2 \times 2 \times 2$ grid for senarmontite and a $2 \times 3 \times 3$ grid for
 139 Sb_2O_5 (Monkhorst and Pack, 1976).

140 Phonon frequencies are computed using linear response theory (Baroni et al., 2001), with the Quantum Espresso
 141 package (Giannozzi et al., 2009). Interatomic force-constants are obtained from the dynamical matrices computed
 142 exactly (within DFT) on a $n \times m \times p$ grid of vectors (where n , m and p are equal to the numbers used for electronic
 143 integration). Long-range effects are taken into account by computing Born effective-charges and static dielectric
 144 constants (Baroni et al., 2001). Dynamical matrices and thus phonon frequencies can be obtained in any point of the

145 reciprocal space by Fourier-interpolation of the force constants. For all materials, the vibrational partition function
146 (Eq. (5)) is converged with a 6×6×6 interpolation grid.

147 To help correlate calculated frequencies at gamma-point with experimental spectroscopic Raman data, the
148 intensities (Raman cross-sections) of each mode are computed for PBEsol calculations. For Raman-active modes,
149 non-resonant Raman cross-sections are computed using second-order response as in Lazzeri and Mauri (2003).

150

151

152 2.3 Raman spectra

153 To directly compare the calculations with the experiment, Raman spectrum configurations of all the structures are
154 modelled for a 300 K temperature (as this temperature was the reference in the experimental valentinite study
155 (Gonçalves et al., 2018)). Two light polarisations are considered: parallel-polarized “xyyx” geometry, with incoming
156 and outgoing polarisation in the same direction (giving A_g modes) and cross-polarized “xyzx” geometry, with
157 incoming and outgoing polarisations perpendicular to each other, giving B_g modes. As the Raman spectra found in
158 the literature are always measured on mineral powders for the cases considered here, the spectra are averaged
159 over several grain orientations (80) and broadened by Gaussian convolution. However, these experimental methods
160 generally give information on anharmonic frequencies at the Brillouin zone center (Méheut-Le Quéau, 2008). So,
161 these comparisons could be biased, but remain the best point of comparison between theoretical and experimental
162 data. Calculated IR frequencies will not be compared for validation of the models with experimental data, as for
163 most of these structures, they do not exist or are incomplete.

164 3. Results

165

166 3.1. Structural predictions

167 The structures of stibnite, valentinite and cervantite are relaxed at the PBE, PBEsol (GGA) and PZ (LDA) levels using
168 the us Sb pseudopotential (Table 1). The calculations using the nc pseudopotential performed for valentinite and
169 cervantite at the PZ and PBESOL levels hold slightly smaller cell parameters (typically by 0.7 %). The results of the us
170 calculations show good agreement with experimental data and previous computations, with global differences
171 under 5 % (Allen et al., 2013; Gopalakrishnan and Manohar, 1975; Kyono and Kimata, 2004; Svensson, 1975). PBE
172 relaxation shows the worst lattice reproduction, with a 8 % deformation along the a -axis for stibnite and valentinite,
173 resulting in an important lattice volume difference. This elongation is not found with the other functionals and
174 particularly for PBEsol, which presents the best agreement with experimental data for each structure, with an
175 average difference of 1 % in the cell parameters for the 3 structures. The comparison between experimental and
176 theoretical data is reported in Table 1 as well as other studies working with similar PBEsol (Ibáñez et al., 2016) and
177 PZ (calculated with semicore, Filip et al., 2013) functionals. Both PBEsol pseudopotentials showed similar lattice
178 values. For the PZ functional, our calculation is reasonably close to the calculation using the pseudopotential w/o
179 semicore (Table 1) while there are significant differences between the two PZ pseudopotentials used in Filip et al.
180 (2013) and this study (Table 1).

181 The Sb-S and Sb-O distances are slightly longer after the relaxation step for all the structures, as in other models
182 (Allen et al., 2013) where the bond elongation ranked between 1 to 4.1 %. No extreme dilatation was reported for
183 the different bonds in the valentinite structure. Despite these small elongations, the bond distances obtained
184 through the calculations are close to measured values and the reproduction of these structures is satisfying to
185 proceed with the next calculation steps.

186 The structures of senarmontite and Sb_2O_5 are calculated at the PBEsol level only (Table 1), based on the conclusion
187 that this functional is the most accurate (see discussion in 3.2).

188 *Table 1: Calculated cell parameters with the different functionals (PBE, PZ, PBESol, us calculations only) determined in this*
 189 *study compared to the experimental data (Expce) and calculations from other authors. Bracketed values are the percentage*
 190 *differences with the experimental data ([†]Kyono et al., 2001, [‡]Whitten et al., 2004, [†]Svensson et al., 1974, [‡]Gopalakrishnan et*
 191 *al., 1975, [×]Jansen 1979) and are compared with other theoretical studies ([‡]Ibáñez et al., 2016 (PBESOL), [‡]Filip et al. 2013*
 192 *(PZ), [‡]Allen et al., 2013 (PBE)).*

Material	Properties	PBE	PZ	—	PBESOL	Expce	Other calculations		
							PBESOL	PZ	PBE
Sb ₂ S ₃ [‡] (Stibnite)	a (Å)	12.199 (+8.1)	10.927 (-3.2)		11.271 (-0.1)	11.282	11.2746 [‡]	11.087 [‡]	
	b (Å)	3.879 (+1.3)	3.786 (-1.1)		3.832 (+0.1)	3.83	3.8306 [‡]	3.838 [‡]	
	c (Å)	11.257 (+0.3)	10.727 (-4.4)		10.916 (-2.8)	11.225	10.8941 [‡]	10.834 [‡]	
	α (°)	90 (0)	90 (0)		90 (0)	90			
	β (°)	90 (0)	90 (0)		90 (0)	90			
	γ (°)	90 (0)	90 (0)		90 (0)	90			
	Sb1-S1 (Å)	2.553 (+1.5)	2.561 (+1.8)		2.590 (+1.8)	2.514			
	Sb1-S2 (Å)	2.574 (+1.4)	2.564 (+1.1)		2.570 (+1.3)	2.537			
	Sb1-S3 (Å)	3.156 (+1.6)	2.979 (-4.1)		3.014 (-3.0)	3.106			
	S2-Sb1-S3 (°)	88.587 (+1.1)	84.183 (-3.9)		85.440 (-2.4)	87.581			
Vol (Å ³)	532.6 (+9.8)	443.8 (-8.5)		471.4 (-2.8)	485				
α-Sb ₂ O ₃ [‡] Senarmontite	a (Å)	-	-		11.130 (+0.1)	11.116			
	α (°)	-	-		90 (0)	90			
	β (°)	-	-		90 (0)	90			
	γ (°)	-	-		90 (0)	90			
	Sb1-O1 (Å)	-	-		2.0195 (+2.0)	1.98			
	Sb1-O2 (Å)	-	-		2.0195 (+2.0)	1.98			
	Sb1-O3 (Å)	-	-		2.0195 (+2.0)	1.98			
	O2-Sb1-O3 (°)	-	-		96.77 (+0.9)	95.87			
	Vol (Å ³)	-	-		1378.78 (+0.3)	1373.55			
β-Sb ₂ O ₃ [†] (Valentinite)	a (Å)	5.323 (+8.6)	4.803 (-2.0)		4.941 (+0.8)	4.9			5.008 [‡]
	b (Å)	12.722 (+2.2)	12.190 (-2.1)		12.296 (-1.2)	12.449			12.654 [‡]
	c (Å)	5.570 (+2.9)	5.372 (-0.7)		5.418 (+0.1)	5.41			5.527 [‡]
	α (°)	90 (0)	90 (0)		90 (0)	90			
	β (°)	90 (0)	90 (0)		90 (0)	90			
	γ (°)	90 (0)	90 (0)		90 (0)	90			
	Sb1-O1 _a (Å)	2.034 (+2.5)	2.008 (+1.2)		2.0228 (+2.0)	1.984			
	Sb1-O1 _b (Å)	2.059 (+1.9)	2.054 (+1.65)		2.0762 (+2.7)	2.021			
	Sb1-O2 (Å)	2.074 (+2.5)	2.068 (+2.2)		2.0624 (+1.9)	2.024			
	Vol (Å ³)	377.2 (+14.3)	314.5 (-4.7)		329.2 (-0.25)	330			350.25 [‡]
α-Sb ₂ O ₄ [‡] (Cervantite)	a (Å)	5.623 (+3.4)	5.455 (+0.4)		5.489 (+1.0)	5.436			5.558 [‡]
	b (Å)	4.940 (+2.7)	4.819 (+0.2)		4.868 (+1.2)	4.81			4.912 [‡]
	c (Å)	12.030 (+2.3)	11.735 (-0.2)		11.819 (+0.5)	11.76			11.943 [‡]
	α (°)	90.0 (0)	90.0 (0)		90.0 (0)	90			
	β (°)	90.0 (0)	90.0 (0)		90.0 (0)	90			
	γ (°)	90.0 (0)	90.0 (0)		90.0 (0)	90			

	Sb1-O1 (Å)	2.030 (+5.3)	1.992 (+3.3)	2.009 (+4.2)	1.929	
	Sb1-O2 (Å)	2.002 (+2.4)	1.965 (+0.5)	1.982 (+1.4)	1.954	
	Sb1-O3 (Å)	2.060 (+1.7)	2.026 (+0.1)	2.042 (+0.8)	2.024	
	O2-Sb1-O3 (°)	88.5 (-2.3)	89.1 (-1.7)	88.9 (-1.9)	90.7	
	Vol (Å ³)	334.2 (+8.7)	308.5 (+0.3)	315.8 (+2.7)	307.5	326.05 ^g
Sb ₂ O ₅ ^x	a (Å)	-	-	12.762 (+0.9)	12.646	
	b (Å)	-	-	3.963 (-17.1)	4.782	
	c (Å)	-	-	3.926 (-27.6)	5.4247	
	α (°)	-	-	87.8 (-2.4)	90	
	β (°)	-	-	101.85 (-2.0)	103.91	
	γ (°)	-	-	91 (+1.1)	90	
	Vol (Å ³)	-	-	194.7 (-38.9)	318.429	

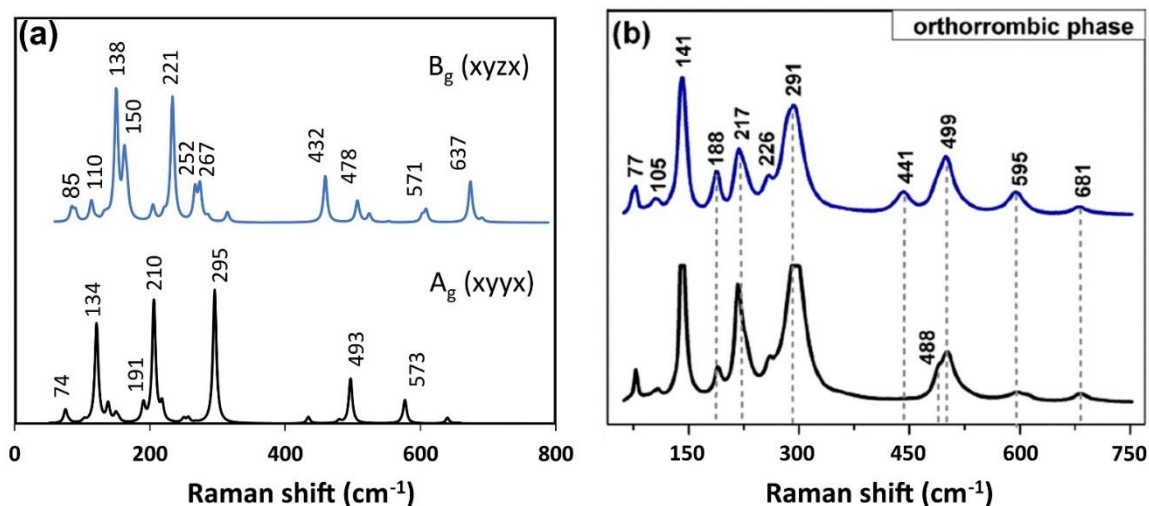
193 3.2 Vibrational predictions

194 To assess the validity of the phonon calculation on the present structures, the calculated vibrational frequencies can
 195 be compared with results from conventional spectroscopic studies (IR and Raman spectra). On classical and well-
 196 known materials commonly used in industries such as stibnite, plenty of experimental and theoretical data are
 197 available on the Raman spectrum (Cai et al., 2018; Ibáñez et al., 2016; Sereni et al., 2010). However, data are not
 198 available or incomplete for rarer materials with no industrial applications, such as senarmontite, cervantite or Sb₂O₅.
 199 For these minerals, the whole spectrum and frequencies are given to provide, for the first time, full calculated
 200 vibrational spectra with their symmetries and they are discussed with previous existing data. PBEsol is the functional
 201 which best suits the experimental frequencies ($R^2 = 0.993$ for all structures). On the other hand, the error of PBE on
 202 frequencies is more variable, especially around the 300 – 600 cm⁻¹ frequencies. The average ~ 4 % underestimation
 203 of the Raman frequencies calculated with PBE observed by Méheut et al. (2007), Scheurer et al. (2014) and Ducher
 204 et al. (2016)) is found as well in this study. However, uncertainties on the cervantite assignation remain high due to
 205 the incompleteness of experimental data. The detailed frequencies and their assignations are discussed below in
 206 details for each mineral considered. Frequencies calculated through nc and us pseudopotentials are close enough to
 207 be associated with each other and to use the Raman intensity calculated with nc to attribute experimental
 208 frequencies to us. All the Raman spectra are calculated with nc pseudopotentials.

209 3.2.1. Stibnite Raman frequencies

210 The calculated Raman frequencies of stibnite are compared to the experimental study from Ibáñez et al. (2016) and
 211 are reported in Table S1. Overall, the theoretical and experimental values are similar, with errors calculated at 0.3 %
 212 with a linear regression between the experimental and theoretical (PBEsol) frequencies. PBEsol best reproduces the
 213 Raman frequencies obtained experimentally (peak positions and symmetries). Frequencies calculated with PZ and
 214 PBEsol show more similarities between each other than with PBE. As stibnite is the most documented Sb mineral
 215 phase and since the experimental and theoretical Raman frequencies have a good correspondence and do not
 216 present any ambiguity, the Raman spectrum of stibnite is not calculated to validate the model nor attribute the
 217 experimental and theoretical frequencies. Calculated Raman frequencies in this study are also compared with
 218 theoretical Raman frequencies from Ibáñez et al., (2016) where PBEsol was used, with a good similarity of lattice
 219 parameters (Table 1). The two theoretical studies show very similar calculated frequencies (Table S1).

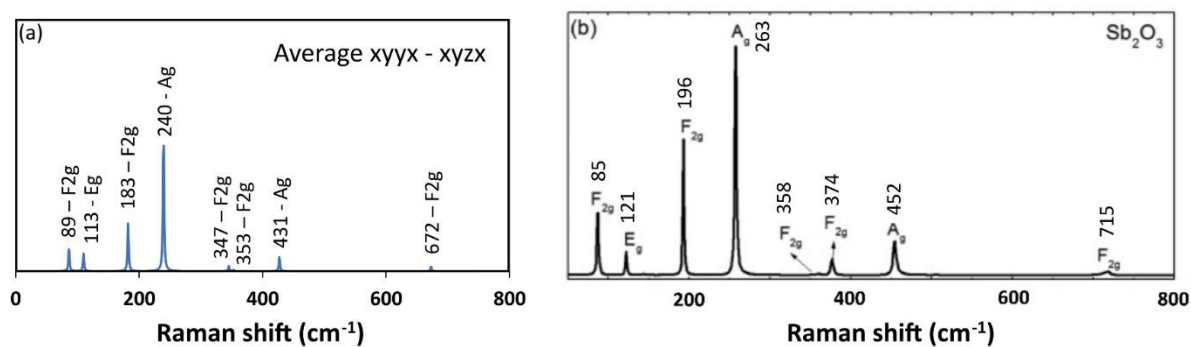
220 3.2.2. Valentinite Raman frequencies



221

222 *Figure 2: a) Raman spectrum of valentinite calculated with the PBEsol functional compared with b) the experimental*
 223 *valentinite Raman spectrum measured at ambient temperature and pressure reproduced from Gonçalves et al. (2018) with*
 224 *permission from Elsevier. Blue lines represent the B_g symmetry while the black represent the A_g symmetry.*

225 The calculated Raman frequencies of valentinite are compared with experimental data from the study of Gonçalves
 226 et al. (2018). The full list of frequencies and symmetries is reported in Table S2 and compared with the experiment.
 227 Then, the Raman spectrum of valentinite is calculated to make the best possible correspondences between the
 228 theoretical and experimental Raman frequencies. For this, the pseudopotential PBEsol_nc is used, as PBEsol gives
 229 the best results for the lattice reproduction. The calculated spectrum is compared with the experimental one in
 230 Figure 2. Some of the experimental frequencies did not find an experimental correspondence (Table S2), however, it
 231 concerns relatively low intensities frequencies (< 100 a.u.) and all the major peaks are attributed to an experimental
 232 equivalent. The errors are acceptable, with -4.4 % for PBEsol compared with the experimental data through linear
 233 regression. As previously seen for lattice parameters, the PBE model is less efficient than the others for Raman
 234 frequencies.



235

236 *Figure 3: a) theoretical Raman spectrum of senarmonite calculated with the PBEsol functional compared with b) the*
 237 *experimental spectrum measured at ambient pressure, reproduced from Pereira et al. (2012) with permission from the*
 238 *American Physical Society.*

239 3.2.3 Senarmonite Raman frequencies

240

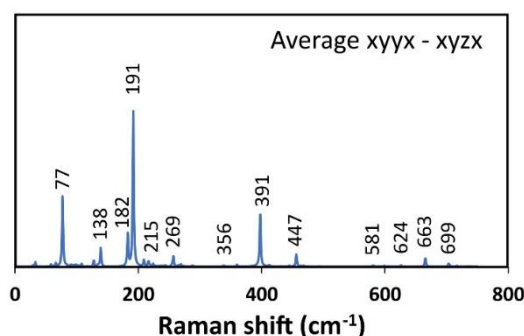
241 The calculated Raman frequencies of senarmonite are compared with the experimental data from Pereira et al.
 242 (2012) at ambient pressure and temperature (Figure 3) and Mestl et al. (1994) (Table S3). As noticed in Pereira et al.
 243 (2012), the E vibration modes calculated were doubly degenerated while the F modes were triply degenerated.

244 Despite some differences with the experimental data (average difference of peak frequency -7.9 % for PBEsol,
 245 Figure 6), the two spectra fit each other relatively well. The theoretical frequency at 305 cm^{-1} (E_g) calculated in this
 246 study had an almost null intensity and cannot be seen in the experimental spectrum presented by Pereira et al.,
 247 (2012) nor in the theoretical spectrum, but is, however, present in the nine Raman frequencies that senarmontite
 248 has and is therefore reported in the theoretical study of Pereira et al., (2012) for the 335 cm^{-1} frequency (Table S3).
 249 Data from Pereira et al., (2012) were similar to the previous Raman frequencies found in the literature (Mestl et al.,
 250 1994).

251 3.2.4 Cervantite Raman frequencies

252 The calculated Raman frequencies of cervantite are compared to the experimental frequencies measured by Cody et
 253 al. (1979) for the validation of the model (Table S4). To attribute the theoretical frequencies to experimental ones,
 254 the average $A_g - B_g$ (xyyx and xyzx polarisations, Figure 4) spectrum is modelled, as symmetries were not given in
 255 Cody et al., (1979) or in any other publication, and the most intense peaks were attributed to the most intense
 256 experimental peaks. These data being old and incomplete made the peak assignment less precise than for the other
 257 structures.

258 To quantify the errors between experimental and theoretical frequencies, the PBEsol model is chosen as a reference
 259 for the symmetries, as this model shows the best correspondence between the experimental and theoretical values
 260 for stibnite and valentinite. With the available data, the theoretical and experimental frequencies are showing good
 261 correspondence with each other (for PBEsol and PZ). The PBE pseudopotential calculations give a negative value (-8
 262 cm^{-1}) as a Raman frequency indicating the inefficiency of PBE compared to PBEsol and PZ. The error between PBEsol
 263 and the experimental data is equal to -2.6% . A particularity of cervantite frequencies compared to the other
 264 structures studied, is that IR shifts also have a Raman component.



265

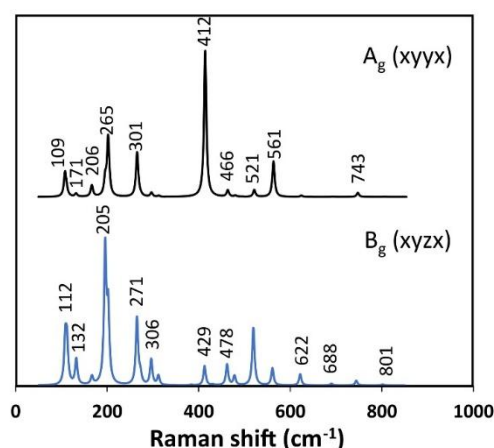
266

Figure 4: Average Raman spectrum of cervantite calculated with the PBEsol functional.

267

268 Experimental frequencies ranged from 43 to 858 cm^{-1} , with higher frequencies ($> 713\text{ cm}^{-1}$) having extremely low
 269 intensities (< 1 arb. unit.). The highest frequency for the theoretical spectrum is around 750 cm^{-1} , which is not in
 270 accordance with the experimental values reported by Cody et al. (1979). This may be attributed to the fact that
 271 measurements made by Cody et al. (1979) recorded some background noise in the high frequencies which were
 272 mistaken with peaks.

273 3.2.5 Sb_2O_5 Raman frequencies



274

275 *Figure 5: Raman spectrum of Sb_2O_5 calculated in this study with the PBEsol functional. The black line represents the A_g*
 276 *symmetry (xyyx) while the blue one represents the B_g symmetry (xyzx).*

277 As PBEsol shows good agreements with experimental data for the previous modelled structures, it is decided to
 278 calculate Sb_2O_5 only with the PBEsol functionals (both us and nc pseudopotentials). No experimental data of the
 279 Raman spectrum of Sb_2O_5 was found in the literature for the validation of the model. The Raman frequencies of
 280 Sb_2O_5 with their intensities are reported in Table S5, as reference for future works implying monoclinic Sb_2O_5 , as for
 281 its Raman spectrum given in Figure 5.

282 3.3. β -factors

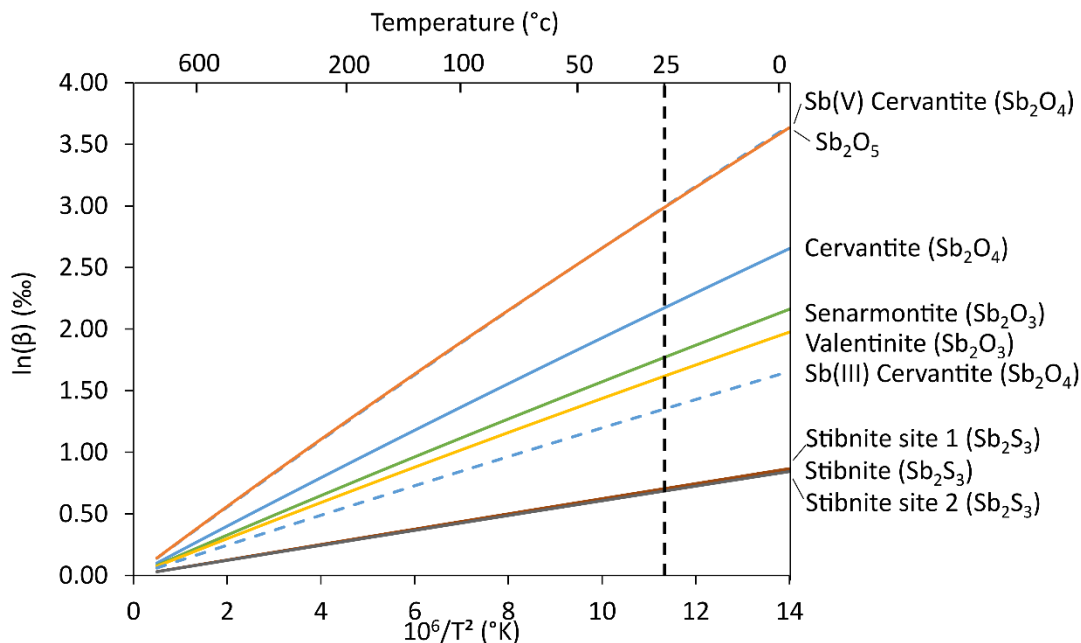
283 *Table 2: Recommended fits of the β -factors calculated for the PBEsol functional with us pseudopotentials and based on an*
 284 *equation of the type $ax^2 + bx^3$, with $x = 10^3/T$ (K).*

Mineral	Temperature range (°C)	Fit parameters	
		a	b
Stibnite	0 - 1100	0.0635	-0.00056
Valentinite	0 - 1100	0.1561	-0.00397
Senarmontite	0 - 1100	0.1719	-0.00454
Cervantite	0 - 1100	0.2256	-0.00603
Sb_2O_5	0 - 1100	0.2960	-0.00964

285

286 The β -factors represent the equilibrium $^{123}Sb/^{121}Sb$ isotopic fractionation factor between the mineral and a
 287 hypothetical perfect gas with the natural average $^{123}Sb/^{121}Sb$ ratio (Méheut-Le Quéau, 2008). The differences
 288 between $\ln(\beta)$ values of the four studied Sb minerals provide an overview of the variability of Sb fractionation
 289 expected in nature (Equation 3). All β -factors are calculated with the PBEsol functional and the us Sb
 290 pseudopotential (Table S6) and the equations describing these fractionations as a function of temperature are listed
 291 in Table 2. The β -factors show significantly different values for the different phases (Figure 6). Stibnite β -factor ($\ln(\beta)$
 292 = 0.71 ‰ at 22 °C) shows a low value compared to valentinite or senarmontite ($\Delta\ln(\beta)_{\text{valentinite-stibnite/senarmontite-stibnite}}$ =
 293 0.93 and 1.09 ‰ at 22 °C, respectively), cervantite ($\Delta\ln(\beta)_{\text{cervantite-stibnite}}$ = 1.49 ‰ at 22 °C) and Sb_2O_5 ($\Delta\ln(\beta)_{\text{Sb2O5-stibnite}}$
 294 = 2.32 ‰ at 22 °C, Figure 6 and Table S6). During the transformation process of these minerals, the different
 295 structures tend to present higher β -factors as they get oxidized ($\beta_{\text{stibnite}} < \beta_{\text{valentinite/senarmontite}} < \beta_{\text{cervantite}} < \beta_{\text{Sb2O5}}$). The
 296 site-by-site calculation for the trivalent and pentavalent Sb forms in cervantite shows that Sb(III) tends to be less
 297 enriched in ^{123}Sb ($\ln(\beta) = 1.37$ ‰ at 22 °C) than Sb(III) in senarmontite ($\ln(\beta) = 1.80$ ‰ at 22 °C) or in valentinite ($\ln(\beta)$
 298 = 1.64 ‰ at 22 °C). On the contrary, the β -factor of Sb(V) in cervantite ($\ln(\beta) = 3.03$ ‰ at 22 °C) is equal to the β -
 299 factor of Sb(V) in pure Sb_2O_5 ($\ln(\beta) = 3.03$ ‰ at 22 °C). Site by site calculations for the two Sb sites in stibnite show

300 very similar β -factor ($\ln(\beta) = 0.696 \text{ ‰}$ at 22 °C for the second site, and 0.716 ‰ for the 1st site), despite a
 301 coordination number lower (3.0 vs 4.1) and shorter bond lengths (2.53 Å vs 2.70 Å) for the second site.



302

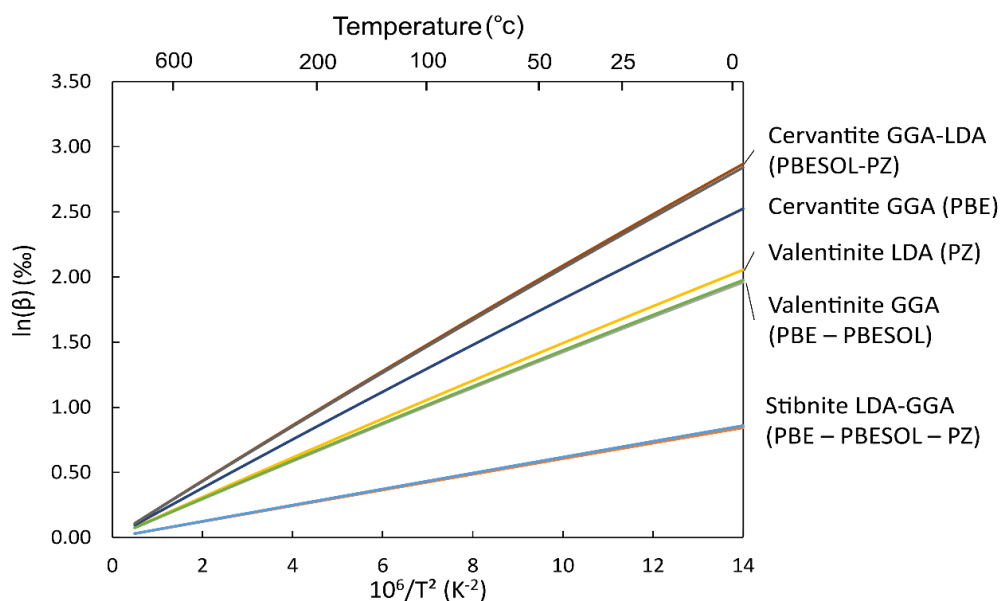
303 *Figure 6: β -factors (in ‰) of the different mineral phases during the oxidation process of the stibnite (Sb_2S_3) to the synthetic*
 304 *fully oxidized mineral phase Sb_2O_5 . These β -factors are calculated with the PBESOL functionals (us pseudopotentials). The*
 305 *Sb(III/V) cervantite (dashed lines) represents the β factor for each individual Sb(III/V) site in cervantite.*

306 3.4 Uncertainties of the β -factors

307

308 To evaluate the uncertainties associated with the β -factors, the calculations are made with LDA (PZ) and GGA
 309 (PBEsol and PBE) functionals. The β -factors calculated with the different functionals are represented in Figure 7 (us
 310 pseudopotentials). The variability between the three functionals is almost null for stibnite, with a difference of 0.02
 311 ‰ between PZ and PBEsol. This difference between the functionals is increasing for valentinite, showing the highest
 312 difference of 0.09 ‰ between PBEsol and PZ. This difference is maximum for cervantite, with a 0.35 ‰ difference
 313 between PBE and PZ, while the difference is only 0.04 ‰ between PBEsol and PZ. These two pseudopotentials show
 314 the most similar atomic structure and vibrational properties (Table 1). The significant difference between PBE and
 315 the two other pseudopotentials could be explained by poorer reliability in the lattice reproduction and theoretical
 316 Raman frequencies for PBE and finally by too high uncertainty. The errors on the Raman frequencies of the
 317 structures are evaluated through a linear regression between the theoretical and experimental frequencies. These
 318 regressions are reported in Figure 8. The errors are evaluated at 0.4 % for stibnite, 3.5 % for valentinite and
 319 cervantite and finally 6.5 % for senarmontite. As demonstrated in appendix B of Méheut et al. (2009), the error on
 320 the logarithmic β -factors given by the errors on the frequencies varies between $n \%$ (low temperature) and $2n \%$
 321 (high temperature). To have only one error per β -factors, the $2n \%$ error will be used to estimate the errors of the
 322 structures. The error attributed to the β -factors are 0 % for stibnite, 7 % for valentinite and cervantite and 16 % for
 323 senarmontite (Table 3).

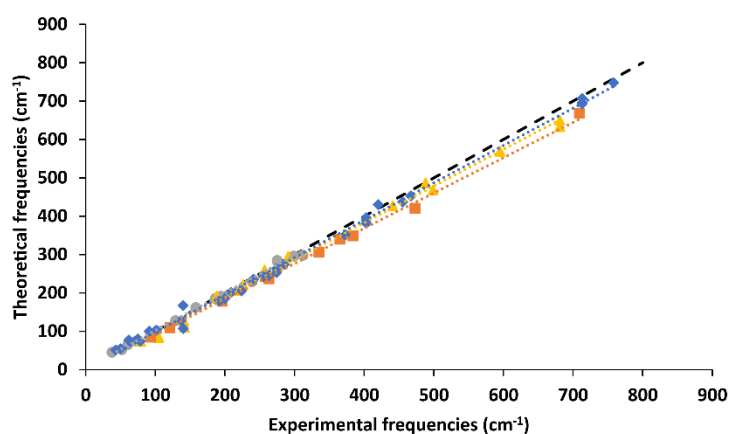
324



325

326 *Figure 7: Comparison of the β -factors calculated using different functionals (GGA (PBE, PBESol) and LDA (PZ)) for three*
 327 *different mineral phases (stibnite (Sb_2S_3), valentinite (Sb_2O_3) and cervantite (Sb_2O_4)).*

328



329

330 *Figure 8: Theoretical Raman frequencies (PBESol functional) as a function of the experimental Raman frequencies of the*
 331 *different studied minerals: stibnite (grey); valentinite (yellow), senarmontite (orange) and cervantite (blue). Linear*
 332 *regressions corresponding to each mineral are represented with dotted lines. The black dashed line represents the 1:1*
 333 *relation.*

334 *Table 3: Raw and corrected β -factors for stibnite, valentinite, senarmontite and cervantite at 22 °C.*

	Stibnite	Valentinite	Senarmontite	Cervantite
Error on Ln(β -factor) (%)	0	7	13	7
Ln(β -factor)	0.71	1.64	1.80	2.20
Corrected Ln(β -factor)	0.71	1.75	2.03	2.35

335

336 As the lattice parameters for stibnite are the least deformed compared with experimental measurements (except
 337 for axis c, composed with Van-Der-Waals bonds), it is consistent that stibnite has the smallest errors on the Raman
 338 frequencies and β -factors. Concerning senarmontite, an error of 13 % on the β -factor is estimated which translates
 339 into an error of 0.23 ‰ at 22°C for $\Delta^{123}Sb_{\text{senarmontite-stibnite}}=1.5$ ‰ and gives an estimate of the precision that can be
 340 expected using such approach.

341 Despite some differences between the various functionals (especially with PBE), all the models show a relatively
 342 good agreement with the experimental results. Only PBE does not show satisfying structural lattice reproduction for
 343 stibnite and valentinite with an important elongation of the a-axis, along with slightly less accurate Raman
 344 frequencies compared to the two other functionals. However, for stibnite, these structural and Raman differences
 345 do not have an impact on the final calculated β -factor. This is not the case for cervantite, where important β -factor
 346 differences are observed between PBE and the two other functionals (PZ and PBEsol).

347 Experimental and theoretical Raman spectrum show similar frequencies, but for cervantite, precise experimental
 348 data about the quality and symmetry of these frequencies are lacking. However, since the previous models (stibnite
 349 and valentinite) show a good correspondence with the data, it can be assumed that it is also the case for cervantite
 350 and Sb_2O_5 , which does not have experimental data to support this theoretical work.

351 The first-principles calculations presented above quantify mass-dependent isotope fractionations originating from
 352 differences in the vibrational properties of the chemical bonds in Sb minerals. However, these calculations did not
 353 take into account the Nuclear Field Shield Effect (NFSE) for Sb nuclei, resulting from differences in volume and
 354 shapes of the atomic nuclei of the different isotopes (Schauble 2007, Fujii *et al.*, 2009). The number of protons is
 355 similar between isotopes of a single element, but their distribution in space within the nuclei can differ. This
 356 difference of size and shape could be represented as the mean-square charge radius $\langle r^2 \rangle$ (Fujii *et al.*, 2009). Usually,
 357 mass fractionation is predominant in light isotopes, while NFSE becomes far more important than mass-dependent
 358 fractionation for the heavy isotopes (e.g. Hg, Tl, U, Yang and Liu, 2016). For Sn, an element close to Sb in terms of
 359 mass and volume, Schauble 2013 demonstrated a limited contribution of NFSE (around 5% of the overall
 360 fractionation). More precisely, the fractionation coming from the NFSE can be written (Almoukhalalati *et al.*, 2016,
 361 in atomic units):

$$\ln\alpha_{NFSE} = \frac{\delta E_{FS}}{kT} = \frac{2\pi Z}{3} * \frac{1}{k * T} * (\bar{\rho}_e^A - \bar{\rho}_e^B) * \Delta\langle r_{123-121}^2 \rangle \quad (7)$$

362 With $\bar{\rho}_e^A$ the effective electronic density in the nuclear volume for chemical species A (in a_0^{-3}), $\Delta\langle r_{123-121}^2 \rangle$ is the
 363 change in mean-square charge radius between ^{123}Sb and ^{121}Sb , $Z=51$ is the number of protons of Sb, $k (=3.16666 \cdot 10^{-6}$
 364 $\text{Ha}\cdot\text{K}^{-1})$ is Boltzmann constant, T is the temperature in K.

365 The parameters controlling the NFSE are therefore the change in effective electronic density $\bar{\rho}_e$ between two
 366 species, and the change in mean-square charge radius (r^2).

367

Equilibrium	Model	$\bar{\rho}_e^A - \bar{\rho}_e^B$ (a_0^3)	$\ln\alpha_{NFSE}^{123-121}\text{Sb}$ at 22°C	$\ln\alpha_{MD}^{123-121}\text{Sb}$ at 22°C (this work)
	CdO (monteponite)- αCd	-15.6		
Sb_2O_5 - Sb_2O_3	SnO_2(cassiterite) -SnO(romachite)	-26.2	-0.075±0.051‰	1.23-1.38‰
	SnO (romachite)- αSn	6.2		
	HgO (montroydite)- αHg	-48.4		
	CdO (monteponite)- CdS (hawleyite)	-4.9		
Sb_2O_3 - Sb_2S_3	SnO(romachite) -SnS	-8.3	-0.024±0.016‰	1.09-0.93‰
	HgO (montroydite)- HgS (cinnabar)	-18.9		

368 *Table 4. Estimates (Schauble 2013) of changes in effective electron density at the nucleus for various equilibria similar to*
 369 *Sb_2O_5 - Sb_2O_3 (oxygen reductions $\text{M}^{n+}\text{O}_{n/2}$ - $\text{Mn}^{(n-2)+}\text{O}_{(n-2)/2}$) or to Sb_2O_3 - Sb_2S_3 (O-S exchanges). In bold are our preferred estimate.*
 370 *$\ln\alpha_{NFSE}^{123-121}\text{Sb}$ (25°C) is calculated from eq. 7 with $\Delta\langle r_{123-121}^2 \rangle = 0.25 \pm 0.17 \cdot 10^{-10} \text{a}_0^2$ (Angeli and Marinova 2013).*
 371 *$\ln\alpha_{MD}^{123-121}\text{Sb}$ is calculated from Table 2 (with Sb_2O_3 taken as valentinite for the first value and senarmontite for the*
 372 *second).*

373 Regarding the change in effective electronic density, to our knowledge, there is no study in the literature
 374 estimating this quantity for Sb species. However, Schauble *et al.* (2013) computed the NFSE effect for various

375 species for Sn, Hg, Tl isotopes. The Sn system is particularly appealing, as it is just before Sb in the periodic
 376 table. As shown in Table 4, we suggest to model the change in effective density for the Sb_2O_5 - Sb_2O_3 equilibrium
 377 with the SnO_2 (cassiterite)- SnO (romachite) equilibrium, and for the Sb_2O_3 - Sb_2S_3 equilibrium with the
 378 SnO (romachite)- SnS equilibrium. The NFSE estimated using these values and the change in nuclear radius
 379 $\Delta\langle r_{123-121}^2 \rangle = 0.25 \pm 0.17 \cdot 10^{-10} a_0^2$ (Angeli and Marinova, 2013) is rather limited (below 5%) with respect to
 380 the conventional mass dependent fractionation. Note that the uncertainty on this effect is rather large due
 381 principally to large uncertainties on the estimate of $\Delta\langle r_{123-121}^2 \rangle$ (Angeli and Marinova, 2013). Other examples
 382 of changes in effective density are given in Table 4, for various other systems. This illustrates that for systems
 383 with similar Z, and for similar equilibria, the corresponding changes in effective densities remain in the same
 384 range as our estimate. As rough as our estimate may be, it is therefore unlikely that NFSE contributes
 385 significantly to the overall Sb fractionation.

386

387 4. Discussion

388 4.1. Parameters controlling the isotopic fractionation

389 The results allow to predict Sb isotope fractionation (direction and amplitude) between different secondary Sb
 390 mineral phases of the oxidation chain of stibnite and to identify the factors responsible for this fractionation. In
 391 order of importance of the magnitude of the induced fractionation, these factors are: the change of Sb oxidation
 392 state, the change of the first neighbour of Sb and the distortion of the atomic Sb - O polyhedron.

393 The change from Sb(III) oxidation state in Sb(III)-phases (valentinite and senarmontite) to mixed Sb(III)/Sb(V)-phase
 394 (cervantite) or Sb(V)-phases (Sb_2O_5) induced an increase of the β -factor. A number of theoretical studies have been
 395 carried out to quantify the equilibrium isotope fractionation between different oxidation states of metals (Cu, Fe,
 396 Mo, Cr, Se, Tl, ...) (Asael et al., 2007; Polyakov and Mineev, 2000; Tossell, 2005). They predicted that oxidized species
 397 are preferentially enriched in heavy isotopes due to the difference in bond length and strength (Asael et al., 2007).
 398 Experimental studies showed the same trend. For Se, oxidative dissolution of selenide-bearing minerals ferroselite
 399 (FeSe_2) and berzelianite (Cu_2Se) produced an enrichment in the heavier isotopes in dissolved Se compared to the
 400 initial minerals, although factors other than redox changes could have been involved in fractionation (e.g.
 401 dissolution, adsorption ...) Wasserman et al. (2021)). Oxidative weathering of crustal Cr(III)-bearing minerals results
 402 in the release of ^{53}Cr -enriched mobile Cr(VI) to the solution (Gilleaudeau et al., 2016). Similar to chromium, redox
 403 transformations between Cu(I) and Cu(II) species are the main processes in natural systems resulting in Cu isotope
 404 fractionation (Little et al., 2017, 2014). For example, reduced and precipitated Cu(I) species are known to be lighter
 405 by 2 ‰ to 5 ‰ relative to dissolved Cu(II) species (Ryan et al., 2014). Among experimental studies dealing with
 406 metal(loid) isotope fractionation related to redox changes, only two were dedicated to Sb. Antimony(V) reduction
 407 experiments were carried out by Rouxel et al. (2003) and showed that this process generated an isotopic
 408 fractionation between oxidized and reduced species $\Delta^{123}\text{Sb}_{\text{Sb(V)-Sb(III)}}$ of about 0.90 ‰. Mackinney (2016) also
 409 observed significant fractionation in the same direction, during the reduction of aqueous Sb(V) by sulphide to form
 410 solid $\text{Sb(III)}_2\text{S}_3$ resulting in a $\Delta^{123}\text{Sb}_{\text{Sb(V)-Sb(III)}_2\text{S}_3}$ of 1.45‰. In this latter study, other factors contributing to Sb isotope
 411 fractionation are probably superimposed to the redox effect, such as the effect of the bounding environment (Sb-Cl
 412 bonds in Sb(V)Cl_5 and Sb-S bonds in Sb_2S_3) and phase change (liquid to solid).

413 The change in the first neighbour of Sb also showed a significant effect on Sb isotopes in the present study. Sb-O
 414 bonds tend to concentrate ^{123}Sb isotope compared to Sb-S bonds. Trivalent atomic Sb-O bonds in cervantite are on
 415 average shorter than trivalent Sb-S bonds in the stibnite (more than 0.6 Å difference, Table 1) and stibnite also has a
 416 higher coordination number for Sb(III) (Figure 1), which could also explain its lower retention of the heavy isotope
 417 (^{123}Sb) compared to Sb-O. The control on fractionation properties can also be explored based on vibrational analysis
 418 (Figure S1, see Meheut et al 2009 for details). The vibrational analysis expresses the contributions of each
 419 vibrational mode to the β -factor. Vibrational analyses for stibnite and valentinite are compared on Figure S1,
 420 showing that most of the Raman frequencies contribute to the β -factor. As a consequence, it is essentially shown
 421 that the higher valentinite β -factor is explained by its generally higher vibrational frequencies, therefore its

422 generally stiffer bonds. Indeed, the heavy isotopes of an element tend to be concentrated in substances where that
 423 element forms the stiffest bonds (Schauble, 2004) and generally the lowest coordination number. Liu et al. (2021) in
 424 a first-principles study about Cu isotopes showed that similar changes from Cu – S to Cu – O structures favoured the
 425 heavy isotope by an increase of the β -factor around 1.2 to 1.8 ‰. Unfortunately, data in the literature are too
 426 scarce to compare the order of magnitude of the modelled Sb isotope fractionation with environmental Sb data.

427 However, there are some apparent discrepancies with respect to these general isotope fractionation rule of thumb.
 428 On average, cervantite has longer Sb – O bonds than valentinite but presents a significantly higher β -factor (> 0.5
 429 ‰), which is clearly contradictory with those tendencies. The relation between the average atomic bond length and
 430 β -factor no longer holds when comparing atomic structures with different atomic bonds, oxidation level and
 431 coordination numbers. The β -factor calculated for trivalent antimony in cervantite on one hand and for pentavalent
 432 antimony in cervantite, on the other hand, showed that pentavalent Sb possesses a higher β -factor than trivalent Sb
 433 in this structure (Figure 6). Thus, the higher enrichment in heavy isotope in cervantite compared to valentinite is
 434 explained by the presence of Sb(V) which makes, on average, the cervantite enriched in the heavy isotope. The
 435 effect of the coexistence of different sites was also studied by Ducher et al. (2016) on the three different Zn sites in
 436 hydrozincite (1 tetra-coordinated and 2 hexa-coordinated sites). The two hexa-coordinated sites were consequently
 437 enriched in heavy isotopes compared with other hexa-coordinated sites of another mineral (smithsonite), between
 438 0.50 to 0.65 ‰ while their Zn – O bond lengths were comparable. This difference was assumed to be caused by the
 439 difference in first-neighbours and the change of partial negative charge of the O atom in hydrozincite caused by the
 440 presence of a hydroxyl group instead of a single O atom.

441 The three trivalent Sb(III) – O phases (senarmontite, valentinite and Sb(III) in cervantite) exhibited slightly different
 442 (more than 0.14 Å) average Sb – O bond length. This difference could be explained by the inclusion of Sb(V) in
 443 cervantite besides Sb(III) or by the adaptation to the orthorhombic cell of the valentinite, which induces a distortion
 444 on the Sb – O polyhedral structure affecting atomic bond lengths, angles and volume, inducing a loss of symmetry
 445 and an increase of the disorder of the structure (Pokrovsky et al., 2014). Nevertheless, these small Sb – O bond
 446 length differences affected only slightly the β -factor.

447 The Sb – S bond lengths and coordination number difference in stibnite between the two Sb sites also shown to
 448 induce very small difference in the β -factor (2 ‰), which is much smaller than variations between the different
 449 atomic dispositions of the Sb₂O₃ minerals and sites.

450

451 4.2. Implications for environmental applications

452 Understanding the parameters controlling isotope fractionation that occurs during different geochemical processes
 453 is an important step for developing the applications of Sb isotopes to sources or processes tracking. This study
 454 provides information on the direction and amplitude of Sb isotope fractionation expected between solid phases that
 455 are important Sb-bearing minerals in the supergene environment. Theoretical Sb isotope fractionation spans over
 456 2.3 ‰ at 22 °C which is similar to the range of isotopic composition observed in natural samples (Rouxel et al., 2003;
 457 Da Wang et al., 2021; Zhai et al., 2021). The studied minerals that compose the stibnite oxidation chain were chosen
 458 because of their ubiquity in the supergene zone, especially in Sb-sulfide mining areas. These minerals play an
 459 essential role in limiting Sb mobility in mining wastes and rivers impacted by mine drainage (Filella et al., 2009;
 460 Roper et al., 2012). All the studied secondary Sb minerals were found to be isotopically heavier than the initial
 461 stibnite. This suggests that the oxidative weathering of sulphide minerals in waste piles could significantly modify
 462 the Sb isotope ratio. This has a strong implication for the application of Sb isotopes as a tracer of contamination
 463 source; a range of Sb isotope signatures of about ~1 ‰ could be expected in a single mining district as a result of
 464 alteration processes. We showed that redox change from Sb(III) to Sb(V) was the transformation that most affected
 465 the Sb isotope composition, by up to 1.2 ‰ (Sb₂O₅ - senarmontite). This supports the idea that Sb isotopes could be
 466 a powerful tracer of redox and paleoredox conditions. The calculated fractionation factor is close to the
 467 fractionation factor observed during experimental reduction of aqueous Sb(V) to Sb(III), which gave $\Delta^{123}\text{Sb}_{\text{Sb(V)-Sb(III)}} =$
 468 0.9 ‰ (Rouxel et al., 2003). Field observations showed the same trend; aqueous Sb(V) in the drainage water of an
 469 Sb mine showed a heavier isotope composition (+ 0.35 ‰) than Sb from the primary stibnite in the mine wastes

470 (Tanimizu et al., 2011). However, a number of processes are superimposed to redox changes under environmental
 471 conditions, that can produce some differences in Sb isotope fractionation factors. Wang et al. (2021) showed that
 472 stibnite precipitation from hydrothermal systems was isotopically lighter than the ore-forming fluid with an $\alpha_{\text{fluid-}}$
 473 stibnite between 0.9991 and 0.9994 ($\Delta^{123}\text{Sb}_{\text{fluid-stibnite}}$ between 0.6 to 0.9 ‰), which is similar to the values reported in
 474 the Table S6 ($\Delta^{123}\text{Sb}_{\text{Sb}_2\text{O}_5\text{-stibnite}} = 0.75$ ‰ at 260 °C, which is within the temperature range of ore formation indicated
 475 in Wang et al. (2021)).

476 Furthermore, the β -factors determined in the present study are calculated with pure phases and perfect Sb – O
 477 structure, with a precise stoichiometric number of Sb sites, which is not the case for natural minerals. Impurities in
 478 the crystal could impact the β -factor by lowering it, through atomic structure distortions (and then Sb – O distances
 479 changes) or, valence modification (Wang et al., 2017; Gao and Liu, 2021). Finally, it is noteworthy that when the
 480 studied transformations occur in the environment, kinetic fractionation processes could alter the isotopic signature
 481 of the mineral, especially during phase change (e.g. solid to liquid).

482 Nevertheless, this study provides trends for Sb isotope behaviour during oxidative dissolution of stibnite and
 483 subsequent precipitation of Sb(III) and Sb(V) oxides in sulphide mining environments (Filella et al., 2009; Resongles
 484 et al., 2013). Secondary minerals of stibnite, such as valentinite and cervantite are expected to have a higher $\delta^{123}\text{Sb}$
 485 signature due to the nature of the atomic bonds (shorter and more energetic). These theoretical data will help in
 486 interpreting Sb isotope signatures along mine waste profiles or mine drainage. Moreover, the results give some
 487 clues for interpreting Sb isotope signature variations in other contaminated contexts such as the urban environment,
 488 where both Sb sulphides and Sb oxides have been evidenced in traffic-related dust (Varrica et al., 2013) and in
 489 natural system, including to better understand isotope variations during Sb ore formation.

490

491 **5. Conclusion**

492 Equilibrium Sb isotopes fractionation factors are calculated from first-principles in minerals involved in the oxidation
 493 process from stibnite to cervantite and a further oxidation step with Sb_2O_5 . Good agreement is obtained between
 494 theoretical and experimental data, showing reliable calculated β -factors. Among the studied minerals, stibnite (Sb_2S_3)
 495 is found to have the lowest β -factor ($\ln(\beta) = 0.71$ ‰ at 22°C) due to the weakest Sb – S bonds, then valentinite ($\ln(\beta)$
 496 = 1.64 ‰ at 22°C), senarmontite ($\ln(\beta) = 1.80$ ‰ at 22°C), cervantite ($\ln(\beta) = 2.20$ ‰ at 22°C) and Sb_2O_5 ($\ln(\beta) = 3.03$
 497 ‰ at 22°C). Such a wide range of variation indicates that the isotopes of this element could be used as a
 498 geochemical tracer. The main factors controlling the isotopic fractionation are found to be, in order of importance,
 499 the oxidation level (Sb(V) is isotopically heavier than Sb(III)), the nature of the atomic bond (Sb – S is isotopically
 500 lighter than Sb – O) and finally, the average bond length between Sb and its first neighbour and structural distortion
 501 of the atomic polyhedron (the most distorted the atomic structure is, the weakest are the atomic bonds). These
 502 calculations represent a first step to understand the geochemical cycle of Sb isotopes in the environment with the
 503 aim to use Sb isotopes for investigating the transformation processes and Sb sources. However, these β -factors
 504 should be considered cautiously in future environmental studies since equilibrium isotopic exchanges can be
 505 disturbed by kinetic fractionation. Nevertheless, these new theoretical data will be useful for future interpretation
 506 of Sb isotope signature in natural or impacted environments and to understand the origin of isotopic variations. This
 507 study could be completed with future studies focused mass dependent isotopic fractionation on Sb aqueous species
 508 or estimating precisely the potential nuclear shield effect of antimony.

509 **Conflicts of interest**

510 There are no conflicts of interest to declare.

511 **Acknowledgements**

512 This work received financial support from the CNRS INSU EC2CO program (Project AntiBol). This work was granted
 513 access to the HPC resources of CALMIP supercomputing center under the allocation Grant P1037-2021.

514 **References**

- 515 Allen, J.P., Carey, J.J., Walsh, A., Scanlon, D.O., Watson, G.W., 2013. Electronic Structures
516 of Antimony Oxides. *J. Phys. Chem. C* 117, 14759–14769.
517 <https://doi.org/10.1021/jp4026249>
- 518 Almoukhalalati, A., Shee, A., Saue, T., 2016. Nuclear size effects in vibrational spectra.
519 *Physical Chemistry Chemical Physics* 18, 15406–15417.
520 <https://doi.org/10.1039/C6CP01913G>
- 521 Angeli, I. and Marinova, K.P. (2013) ‘Table of experimental nuclear ground state charge radii:
522 An update’, *Atomic Data and Nuclear Data Tables*, 99(1), pp. 69–95. Available at:
523 <https://doi.org/10.1016/j.adt.2011.12.006>.
- 524 Asael, D., Matthews, A., Bar-Matthews, M., Halicz, L., 2007. Copper isotope fractionation in
525 sedimentary copper mineralization (Timna Valley, Israel). *Chemical Geology* 243,
526 238–254. <https://doi.org/10.1016/j.chemgeo.2007.06.007>
- 527 Ashley, P.M., Craw, D., Graham, B.P., Chappell, D.A., 2003. Environmental mobility of
528 antimony around mesothermal stibnite deposits, New South Wales, Australia and
529 southern New Zealand. *Journal of Geochemical Exploration* 77, 1–14.
530 [https://doi.org/10.1016/S0375-6742\(02\)00251-0](https://doi.org/10.1016/S0375-6742(02)00251-0)
- 531 Aufmuth, P., Heilig, K. and Steudel, A. (1987) ‘Changes in mean-square nuclear charge radii
532 from optical isotope shifts’, *Atomic Data and Nuclear Data Tables*, 37(3), pp. 455–490.
533 Available at: [https://doi.org/10.1016/0092-640X\(87\)90028-3](https://doi.org/10.1016/0092-640X(87)90028-3).
- 534 Baroni, S., de Gironcoli, S., Dal Corso, A., Giannozzi, P., 2001. Phonons and related crystal
535 properties from density-functional perturbation theory. *Rev. Mod. Phys.* 73, 515–562.
536 <https://doi.org/10.1103/RevModPhys.73.515>
- 537 Bigeleisen, J., Mayer, M.G., 1947. Calculation of Equilibrium Constants for Isotopic
538 Exchange Reactions. *J. Chem. Phys.* 15, 261–267. <https://doi.org/10.1063/1.1746492>
- 539 Cai, Y., Yang, C., Xu, D., Gui, W., 2018. Quantitative analysis of stibnite content in a raw ore
540 by Raman spectroscopy and chemometric tools. *Journal of Raman spectroscopy* 50,
541 454–464. <https://doi.org/10.1002/jrs.5527>
- 542 Chang, T.-L., Qian, Q.-Y., Zhao, M.-T., Wang, J., 1993. The isotopic abundance of antimony.
543 *International Journal of Mass Spectrometry and Ion Processes* 123, 77–82.
544 [https://doi.org/10.1016/0168-1176\(93\)87056-X](https://doi.org/10.1016/0168-1176(93)87056-X)
- 545 Cheema, A.I., Liu, G., Yousaf, B., Abbas, Q., Zhou, H., 2020. A comprehensive review of
546 biogeochemical distribution and fractionation of lead isotopes for source tracing in
547 distinct interactive environmental compartments. *Science of The Total Environment*
548 719, 135658. <https://doi.org/10.1016/j.scitotenv.2019.135658>
- 549 Cody, C.A., Dicarolo, L., Darlington, R.K., 1979. Vibrational and Thermal Study of Antimony
550 Oxides. *Inorganic Chemistry* 18, 1572–1576. <https://doi.org/10.1021/1572-1576>
- 551 Dal Corso, A., 2014. Pseudopotentials periodic table : From H to Pu. *Computational Materials
552 Science* 95, 337–350. <http://dx.doi.org/10.1016/j.commatsci.2014.07.043>
- 554 Degryse, P., Lobo, L., Shortland, A., Vanhaecke, F., Blomme, A., Painter, J., Gimeno, D.,
555 Eremin, K., Greene, J., Kirk, S., Walton, M., 2015. Isotopic investigation into the raw
556 materials of Late Bronze Age glass making. *Journal of Archaeological Science* 62,
557 153–160. <https://doi.org/10.1016/j.jas.2015.08.004>
- 558 Degryse, P., Shortland, A.J., Dillis, S., van Ham-Meert, A., Vanhaecke, F., Leeming, P., 2020.
559 Isotopic evidence for the use of Caucasian antimony in Late Bronze Age glass making.
560 *Journal of Archaeological Science* 120, 105195.
561 <https://doi.org/10.1016/j.jas.2020.105195>

- 562 Dillis, S., Ham-Meert, A.V., Leeming, P., Shortland, A., Gobejishvili, G., Abramishvili, M.,
563 Degryse, P., 2019. Antimony as a raw material in ancient metal and glass making:
564 provenancing Georgian LBA metallic Sb by isotope analysis. *STAR: Science &*
565 *Technology of Archaeological Research* 5, 1–15.
566 <https://doi.org/10.1080/20548923.2019.1681138>
- 567 Ducher, M., Blanchard, M., Balan, E., 2016. Equilibrium zinc isotope fractionation in Zn-
568 bearing minerals from first-principles calculations. *Chemical Geology* 443, 87–96.
569 <https://doi.org/10.1016/j.chemgeo.2016.09.016>
- 570 Filella, M., Philippo, S., Belzile, N., Chen, Y., Quentel, F., 2009. Natural attenuation
571 processes applying to antimony: A study in the abandoned antimony mine in Goesdorf,
572 Luxembourg. *Science of The Total Environment* 407, 6205–6216.
573 <https://doi.org/10.1016/j.scitotenv.2009.08.027>
- 574 Filip, M.R., Patrick, C.E., Giustino, F., 2013. GW quasiparticle band structures of stibnite,
575 antimonselite, bismuthinite, and guanajuatite. *Phys. Rev. B* 87, 205125.
576 <https://doi.org/10.1103/PhysRevB.87.205125>
- 577 Fujii, T. et al. (2009) ‘Mass-Dependent and Mass-Independent Isotope Effects of Zinc in a
578 Redox Reaction’, *The Journal of Physical Chemistry A*, 113(44), pp. 12225–12232.
579 Available at: <https://doi.org/10.1021/jp904882d>.
- 580 Fujii, T., Moynier, F., Blichert-Toft, J., Albarède, F., 2014. Density functional theory
581 estimation of isotope fractionation of Fe, Ni, Cu, and Zn among species relevant to
582 geochemical and biological environments. *Geochimica et Cosmochimica Acta* 140,
583 553–576. <https://doi.org/10.1016/j.gca.2014.05.051>
- 584 Gamrath, S. et al. (2018) ‘MCDHF calculations of isotope shifts in neutral antimony’, *Journal*
585 *of Quantitative Spectroscopy and Radiative Transfer*, 218, pp. 38–45. Available at:
586 <https://doi.org/10.1016/j.jqsrt.2018.07.004>.
- 587 Gao, C., Liu, Y., 2021. First-principles calculations of equilibrium bromine isotope
588 fractionations. *Geochimica et Cosmochimica Acta* 297, 65–81.
589 <https://doi.org/10.1016/j.gca.2021.01.010>
- 590 Giannozzi, P., Andreussi, O., Brumme, T., Bunau, O., Nardelli, M.B., Calandra, M., Car, R.,
591 Cavazzoni, C., Ceresoli, D., Cococcioni, M., Colonna, N., Carnimeo, I., Corso, A.D.,
592 Gironcoli, S. de, Delugas, P., DiStasio, R.A., Ferretti, A., Floris, A., Fratesi, G.,
593 Fugallo, G., Gebauer, R., Gerstmann, U., Giustino, F., Gorni, T., Jia, J., Kawamura,
594 M., Ko, H.-Y., Kokalj, A., Küçükbenli, E., Lazzeri, M., Marsili, M., Marzari, N.,
595 Mauri, F., Nguyen, N.L., Nguyen, H.-V., Otero-de-la-Roza, A., Paulatto, L., Poncé, S.,
596 Rocca, D., Sabatini, R., Santra, B., Schlipf, M., Seitsonen, A.P., Smogunov, A.,
597 Timrov, I., Thonhauser, T., Umari, P., Vast, N., Wu, X., Baroni, S., 2017. Advanced
598 capabilities for materials modelling with Quantum ESPRESSO. *J. Phys.: Condens.*
599 *Matter* 29, 465901. <https://doi.org/10.1088/1361-648X/aa8f79>
- 600 Giannozzi, P., Baroni, S., Bonini, N., Calandra, M., Car, R., Cavazzoni, C., Ceresoli, D.,
601 Chiarotti, G.L., Cococcioni, M., Dabo, I., Corso, A.D., Gironcoli, S. de, Fabris, S.,
602 Fratesi, G., Gebauer, R., Gerstmann, U., Gougoussis, C., Kokalj, A., Lazzeri, M.,
603 Martin-Samos, L., Marzari, N., Mauri, F., Mazzarello, R., Paolini, S., Pasquarello, A.,
604 Paulatto, L., Sbraccia, C., Scandolo, S., Sclauzero, G., Seitsonen, A.P., Smogunov, A.,
605 Umari, P., Wentzcovitch, R.M., 2009. QUANTUM ESPRESSO: a modular and open-
606 source software project for quantum simulations of materials. *J. Phys.: Condens.*
607 *Matter* 21, 395502. <https://doi.org/10.1088/0953-8984/21/39/395502>
- 608 Gilleaudeau, G.J., Frei, R., Kaufman, A.J., Kah, L.C., Azmy, K., Bartley, J.K., Chernyavskiy,
609 P., Knoll, A.H., 2016. Oxygenation of the mid-Proterozoic atmosphere: clues from
610 chromium isotopes in carbonates. *Geochemical Perspectives Letters* 2, 178–187.
611 <https://doi.org/10.7185/geochemlet.1618>

- 612 Gonçalves, R.A., Baldan, M.R., Chiquito, A.J., Berengue, O.M., 2018. Synthesis of
613 orthorhombic Sb₂O₃ branched rods by a vapor–solid approach. *Nano-Structures &*
614 *Nano-Objects* 16, 127–133. <https://doi.org/10.1016/j.nanoso.2018.05.008>
- 615 Gopalakrishnan, P., Manohar, H., 1975. Cervantite, Alpha -Sb₂O₄. *Cryst. Struct. Communic.*
- 616 He, M., Wang, N., Long, X., Zhang, C., Ma, C., Zhong, Q., Wang, A., Pervaiz, A., Shan, J.,
617 2019. Antimony speciation in the environment: Recent advances in understanding the
618 biogeochemical processes and ecological effects. *Journal of Environmental Sciences*
619 75, 14–39. <https://doi.org/10.1016/j.jes.2018.05.023>
- 620 Hiller, E., Lalinská, B., Chovan, M., Jurkovič, Ľ., Klimko, T., Jankulár, M., Hovorič, R.,
621 Šottník, P., Fláková, R., Ženišová, Z., Ondrejková, I., 2012. Arsenic and antimony
622 contamination of waters, stream sediments and soils in the vicinity of abandoned
623 antimony mines in the Western Carpathians, Slovakia. *Applied Geochemistry* 27,
624 598–614. <https://doi.org/10.1016/j.apgeochem.2011.12.005>
- 625 Ibáñez, J., Sans, J.A., Popescu, C., López-Vidrier, J., Elvira-Betanzos, J.J., Cuenca-Gotor,
626 V.P., Gomis, O., Manjón, F.J., Rodríguez-Hernández, P., Muñoz, A., 2016a.
627 Structural, Vibrational, and Electronic Study of Sb₂S₃ at High Pressure. *J. Phys.*
628 *Chem. C* 120, 10547–10558. <https://doi.org/10.1021/acs.jpcc.6b01276>
- 629 Ibáñez, J., Sans, J.A., Popescu, C., López-Vidrier, J., Elvira-Betanzos, J.J., Cuenca-Gotor,
630 V.P., Gomis, O., Manjón, F.J., Rodríguez-Hernández, P., Muñoz, A., 2016b.
631 Structural, Vibrational, and Electronic Study of Sb₂S₃ at High Pressure. *J. Phys.*
632 *Chem. C* 120, 10547–10558. <https://doi.org/10.1021/acs.jpcc.6b01276>
- 633 Jansen, M., 1979. Preparation and crystal structure of antimony oxyde hydrate (Sb₂O₅.
634 3/5H₂O ; SB5O12 (OH).H₂O). *Acta Crystallographica, Section B* 35, 539–542.
- 635 Komárek, M., Ratič, G., Vaňková, Z., Šípková, A., Chrástný, V., 2021. Metal isotope
636 complexation with environmentally relevant surfaces: Opening the isotope
637 fractionation black box. *Critical Reviews in Environmental Science and Technology*
638 1–31. <https://doi.org/10.1080/10643389.2021.1955601>
- 639 Kyono, A., Kimata, M., 2004. Structural variations induced by difference of the inert pair
640 effect in the stibnite-bismuthinite solid solution series (Sb,Bi)₂S₃. *American*
641 *Mineralogist* 89, 932–940. <https://doi.org/10.2138/am-2004-0702>
- 642 Lazzeri, M., Mauri, F., 2003. First-Principles Calculation of Vibrational Raman Spectra in
643 Large Systems: Signature of Small Rings in Crystalline SiO₂. *Phys. Rev. Lett.* 90,
644 036401. <https://doi.org/10.1103/PhysRevLett.90.036401>
- 645 Little, S.H., Sherman, D.M., Vance, D., Hein, J.R., 2014. Molecular controls on Cu and Zn
646 isotopic fractionation in Fe–Mn crusts. *Earth and Planetary Science Letters* 396, 213–
647 222. <https://doi.org/10.1016/j.epsl.2014.04.021>
- 648 Little, S.H., Vance, D., McManus, J., Severmann, S., Lyons, T.W., 2017. Copper isotope
649 signatures in modern marine sediments. *Geochimica et Cosmochimica Acta* 212, 253–
650 273. <https://doi.org/10.1016/j.gca.2017.06.019>
- 651 Liu, F., Le, X.C., McKnight-Whitford, A., Xia, Y., Wu, F., Elswick, E., Johnson, C.C., Zhu,
652 C., 2010. Antimony speciation and contamination of waters in the Xikuangshan
653 antimony mining and smelting area, China. *Environ Geochem Health* 32, 401–413.
654 <https://doi.org/10.1007/s10653-010-9284-z>
- 655 Liu, S., Li, Y., Liu, Jie, Yang, Z., Liu, Jianming, Shi, Y., 2021. Equilibrium Cu isotope
656 fractionation in copper minerals: a first-principles study. *Chemical Geology* 564,
657 120060. <https://doi.org/10.1016/j.chemgeo.2021.120060>
- 658 Lobo, L., Degryse, P., Shortland, A., Eremin, K., Vanhaecke, F., 2014. Copper and antimony
659 isotopic analysis via multi-collector ICP-mass spectrometry for provenancing ancient
660 glass. *Journal of Analytical Atomic Spectrometry* 29, 58–64.
661 <https://doi.org/10.1039/C3JA50303H>

- 662 Lobo, L., Degryse, P., Shortland, A., Vanhaecke, F., 2013. Isotopic analysis of antimony
663 using multi-collector ICP-mass spectrometry for provenance determination of Roman
664 glass. *Journal of Analytical Atomic Spectrometry* 28, 1213–1219.
665 <https://doi.org/10.1039/c3ja50018g>
- 666 Mackinney, J.S., 2016. Antimony isotopes as indicator of RedOx reactions in aqueous
667 systems: fractionation during Sb(V) reduction by sulfide and isotope exchange
668 kinetics between dissolved Sb(III) and Sb(V) (Thesis). University of Illinois at
669 Urbana-Champaign.
- 670 Méheut, M., Lazzeri, M., Balan, E., Mauri, F., 2009. Structural control over equilibrium
671 silicon and oxygen isotopic fractionation: A first-principles density-functional theory
672 study. *Chemical Geology, Applications of non-traditional stable isotopes in high-*
673 *temperature geochemistry* 258, 28–37. <https://doi.org/10.1016/j.chemgeo.2008.06.051>
- 674 Méheut, M., Lazzeri, M., Balan, E., Mauri, F., 2007a. Equilibrium isotopic fractionation in
675 the kaolinite, quartz, water system: Prediction from first-principles density-functional
676 theory. *Geochimica et Cosmochimica Acta* 71, 3170–3181.
677 <https://doi.org/10.1016/j.gca.2007.04.012>
- 678 Méheut, M., Lazzeri, M., Balan, E., Mauri, F., 2007b. Equilibrium isotopic fractionation in
679 the kaolinite, quartz, water system: Prediction from first-principles density-functional
680 theory. *Geochimica et Cosmochimica Acta* 71, 3170–3181.
681 <https://doi.org/10.1016/j.gca.2007.04.012>
- 682 Méheut-Le Quéau, M., 2008. Calcul prédictif du facteur de partage isotopique entre minéraux
683 dans le cadre de la théorie de la fonctionnelle de la densité (phdthesis). Université
684 Pierre et Marie Curie - Paris VI.
- 685 Méheut, M., Ibañez-Mejía, M. and Tissot, F.L.H. (2021) ‘Drivers of zirconium isotope
686 fractionation in Zr-bearing phases and melts: The roles of vibrational, nuclear field
687 shift and diffusive effects’, *Geochimica et Cosmochimica Acta*, 292, pp. 217–234.
688 Available at: <https://doi.org/10.1016/j.gca.2020.09.028>.
- 689 Mestl, G., Ruiz, P., Delmon, B., Knözinger, H., 1994. Sb₂O₃/Sb₂O₄ in Reducing/oxidizing
690 Environments: An in Situ Raman Spectroscopy Study. *Journal of Physical Chemistry*
691 11276–11282. [https://doi.org/0022-3654/94/2098-11276\\$04.50/0](https://doi.org/0022-3654/94/2098-11276$04.50/0)
- 692 Mestl, G., Ruiz, P., Delmon, B., Knözinger, H., n.d. Sb₂O₃/Sb₂O₄ in Reducing/oxidizing
693 Environments: An in Situ Raman Spectroscopy Study. *Journal of Physical Chemistry*
694 1994, 11276–11282. [https://doi.org/0022-3654/94/2098-11276\\$04.50/0](https://doi.org/0022-3654/94/2098-11276$04.50/0)
- 695 Momma, K., Izumi, F., 2011. VESTA 3 for three-dimensional visualization of crystal,
696 volumetric and morphology data. *J Appl Cryst* 44, 1272–1276.
697 <https://doi.org/10.1107/S0021889811038970>
- 698 Monkhorst, H.J., Pack, J.D., 1976. Special points for Brillouin-zone integrations. *Phys. Rev.*
699 *B* 13, 5188–5192. <https://doi.org/10.1103/PhysRevB.13.5188>
- 700 Moynier, F., Fujii, T. and Telouk, P. (2009) ‘Mass-independent isotopic fractionation of tin in
701 chemical exchange reaction using a crown ether’, *Analytica Chimica Acta*, 632(2), pp.
702 234–239. Available at: <https://doi.org/10.1016/j.aca.2008.11.015>.
- 703 Moynier, F., Vance, D., Fujii, T., Savage, P., 2017. The Isotope Geochemistry of Zinc and
704 Copper. *Reviews in Mineralogy and Geochemistry* 82, 543–600.
705 <https://doi.org/10.2138/rmg.2017.82.13>
- 706 Perdew, J.P., Burke, K., Ernzerhof, M., 1996. Generalized Gradient Approximation Made
707 Simple. *Phys. Rev. Lett.* 77, 3865–3868. <https://doi.org/10.1103/PhysRevLett.77.3865>
- 708 Perdew, J.P., Ruzsinszky, A., Csonka, G.I., Vydrov, O.A., Scuseria, G.E., Constantin, L.A.,
709 Zhou, X., Burke, K., 2008. Restoring the Density-Gradient Expansion for Exchange in
710 Solids and Surfaces. *Phys. Rev. Lett.* 100, 136406.
711 <https://doi.org/10.1103/PhysRevLett.100.136406>

- 712 Perdew, J.P., Zunger, A., 1981. Self-interaction correction to density-functional
713 approximations for many-electron systems. *Phys. Rev. B* 23, 5048–5079.
714 <https://doi.org/10.1103/PhysRevB.23.5048>
- 715 Pereira, A.L.J., Gracia, L., Santamaría-Pérez, D., Vilaplana, R., Manjón, F.J., Errandonea, D.,
716 Nalin, M., Beltrán, A., 2012. Structural and vibrational study of cubic Sb₂O₃ under
717 high pressure. *Phys. Rev. B* 85, 174108. <https://doi.org/10.1103/PhysRevB.85.174108>
- 718 Pokrovsky, O.S., Galy, A., Schott, J., Pokrovski, G.S., Mantoura, S., 2014. Germanium
719 isotope fractionation during Ge adsorption on goethite and its coprecipitation with Fe
720 oxy(hydr)oxides. *Geochimica et Cosmochimica Acta* 131, 138–149.
721 <https://doi.org/10.1016/j.gca.2014.01.023>
- 722 Polyakov, V.B., Mineev, S.D., 2000. The use of Mössbauer spectroscopy in stable isotope
723 geochemistry. *Geochimica et Cosmochimica Acta* 64, 849–865.
724 [https://doi.org/10.1016/S0016-7037\(99\)00329-4](https://doi.org/10.1016/S0016-7037(99)00329-4)
- 725 Resongles, E., Casiot, C., Elbaz-Poulichet, F., Freyrier, R., Bruneel, O., Piot, C., Delpoux, S.,
726 Volant, A., Desoeuvre, A., 2013. Fate of Sb(V) and Sb(III) species along a gradient of
727 pH and oxygen concentration in the Canoules mine waters (Southern France).
728 *Environmental Science Processes and Impacts* 15, 1536–1544.
729 <https://doi.org/10.1039/c3em00215b>
- 730 Resongles, E., Freyrier, R., Casiot, C., Viers, J., Chmeleff, J., Elbaz-Poulichet, F., 2015.
731 Antimony isotopic composition in river waters affected by ancient mining activity.
732 *Talanta* 144, 851–861. <http://dx.doi.org/10.1016/j.talanta.2015.07.013>
- 733 Roper, A.J., Willials, P.A., Montserrat, F., 2012a. Secondary antimony minerals: Phases that
734 control the dispersion of antimony in the supergene zone. *Chimie der Erde* 72, 9–14.
- 735 Roper, A.J., Willials, P.A., Montserrat, F., 2012b. Secondary antimony minerals: Phases that
736 control the dispersion of antimony in the supergene zone. *Chimie der Erde* 72, 9–14.
- 737 Rouxel, O., Ludden, J., Fouquet, Y., 2003. Antimony isotope variations in natural systems
738 and implications for their use as geochemical tracers. *Chemical Geology* 200, 25–40.
739 [https://doi.org/10.1016/S0009-2541\(03\)00121-9](https://doi.org/10.1016/S0009-2541(03)00121-9)
- 740 Ryan, B.M., Kirby, J.K., Degryse, F., Scheiderich, K., McLaughlin, M.J., 2014. Copper
741 Isotope Fractionation during Equilibration with Natural and Synthetic Ligands.
742 *Environ. Sci. Technol.* 48, 8620–8626. <https://doi.org/10.1021/es500764x>
- 743 Schauble, E.A., 2004. Applying Stable Isotope Fractionation Theory to New Systems.
744 *Reviews in Mineralogy and Geochemistry* 55, 65–111.
745 <https://doi.org/10.2138/gsrmg.55.1.65>
- 746 Schauble, E.A. (2007) ‘Role of nuclear volume in driving equilibrium stable isotope
747 fractionation of mercury, thallium, and other very heavy elements’, *Geochimica et*
748 *Cosmochimica Acta*, 71(9), pp. 2170–2189. <https://doi.org/10.1016/j.gca.2007.02.004>.
- 749 Schauble, E.A., Méheut, M., Hill, P.S., 2009. Combining Metal Stable Isotope Fractionation
750 Theory with Experiments. *Elements* 5, 369–374.
751 <https://doi.org/10.2113/gselements.5.6.369>
- 752 Schauble, E.A. (2013) ‘Modeling nuclear volume isotope effects in crystals’, *Proceedings of*
753 *the National Academy of Sciences*, 110(44), pp. 17714–17719.
754 <https://doi.org/10.1073/pnas.1216216110>.
- 755 Scheurer, M., Schmutz, B., Happel, O., Brauch, H.-J., Wüsler, R., Storck, F.R., 2014.
756 Transformation of the artificial sweetener acesulfame by UV light. *Science of the*
757 *Total Environment* 425–432. <http://dx.doi.org/10.1016/j.scitotenv.2014.02.047>
- 758 Sereni, P., Musso, M., Knoll, P., Blaha, P., Schwarz, K., Schmidt, G., 2010. Polarization-
759 Dependent Raman Characterization of Stibnite (Sb₂S₃).
- 760 Sherman, D.M., 2013. Equilibrium isotopic fractionation of copper during oxidation/reduction,
761 aqueous complexation and ore-forming processes: Predictions from hybrid density

- 762 functional theory. *Geochimica et Cosmochimica Acta* 118, 85–97.
763 <https://doi.org/10.1016/j.gca.2013.04.030>
- 764 Sundar, S., Chakravarty, 2010. Antimony Toxicity. *International Journal of Environmental*
765 *Research and Public Health* 7, 4267–4277. <https://doi.org/10.3390/ijerph7124267>
- 766 Svensson, C., 1975. Refinement of the crystal structure of cubic antimony trioxide, Sb₂O₃.
767 *Acta Cryst B* 31, 2016–2018. <https://doi.org/10.1107/S0567740875006759>
- 768 Tanimizu, M., Araki, Y., Asaoka, S., Takahashi, Y., 2011. Determination of natural isotopic
769 variation in antimony using inductively coupled plasma mass spectrometry for an
770 uncertainty estimation of the standard atomic weight of antimony. *Geochemical*
771 *Journal* 45, 27–32.
- 772 Tian, H., Zhou, J., Zhu, C., Zhao, D., Gao, J., Hao, J., He, M., Liu, K., Wang, K., Hua, S.,
773 2014. A Comprehensive Global Inventory of Atmospheric Antimony Emissions from
774 Anthropogenic Activities, 1995–2010. *Environ. Sci. Technol.* 48, 10235–10241.
775 <https://doi.org/10.1021/es405817u>
- 776 Tossell, J.A., 2005. Calculating the partitioning of the isotopes of Mo between oxidic and
777 sulfidic species in aqueous solution. *Geochimica et Cosmochimica Acta* 69, 2981–
778 2993. <https://doi.org/10.1016/j.gca.2005.01.016>
- 779 Urey, H.C., 1947. The thermodynamic properties of isotopic substances. *J. Chem. Soc.* 562–
780 581. <https://doi.org/10.1039/JR9470000562>
- 781 Varrica, D., Bardelli, F., Dongarrà, G., Tamburo, E., 2013. Speciation of Sb in airborne
782 particulate matter, vehicle brake linings, and brake pad wear residues. *Atmospheric*
783 *Environment* 64, 18–24. <https://doi.org/10.1016/j.atmosenv.2012.08.067>
- 784 Wang, Da, Mathur, R., Zheng, Y., Qiu, K., Wu, H., 2021. Redox-controlled antimony isotope
785 fractionation in the epithermal system: New insights from a multiple metal stable
786 isotopic combination study of the Zhaxikang Sb–Pb–Zn–Ag deposit in Southern Tibet.
787 *Chemical Geology* 584, 120541. <https://doi.org/10.1016/j.chemgeo.2021.120541>
- 788 Wang, D., Zheng, Y., Mathur, R., Ren, H., 2021. Sulfur isotopic characteristics of the
789 Zhaxikang Sb–Pb–Zn–Ag deposit in southern Tibet. *Australian Journal of Earth*
790 *Sciences* 68, 120–130. <https://doi.org/10.1080/08120099.2020.1762738>
- 791 Wang, W., Qin, T., Zhou, C., Huang, S., Wu, Z., Huang, F., 2017. Concentration effect on
792 equilibrium fractionation of Mg–Ca isotopes in carbonate minerals: Insights from first-
793 principles calculations. *Geochimica et Cosmochimica Acta* 208, 185–197.
794 <https://doi.org/10.1016/j.gca.2017.03.023>
- 795 Wasserman, N.L., Schilling, K., Johnson, T.M., Pallud, C., 2021. Selenium Isotope Shifts
796 during the Oxidation of Selenide-Bearing Minerals. *ACS Earth Space Chem.* 5, 1140–
797 1149. <https://doi.org/10.1021/acsearthspacechem.1c00036>
- 798 Whitten, A.E., Dittrich, B., Spackman, M.A., Turner, P., Brown, T.C., 2004. Charge density
799 analysis of two polymorphs of antimony(III) oxide. *Dalton Trans.* 23–29.
800 <https://doi.org/10.1039/B312550E>
- 801 Wiederhold, J.G., 2015. Metal Stable Isotope Signatures as Tracers in Environmental
802 Geochemistry. *Environ. Sci. Technol.* 49, 2606–2624.
803 <https://doi.org/10.1021/es504683e>
- 804 Yang, S. and Liu, Y. (2016) ‘Nuclear field shift effects on stable isotope fractionation: a
805 review’, *Acta Geochimica*, 35(3), pp. 227–239. Available at:
806 <https://doi.org/10.1007/s11631-016-0109-3>.
- 807 Zhai, D., Mathur, R., Liu, S.-A., Liu, J., Godfrey, L., Wang, K., Xu, J., Vervoort, J., 2021.
808 Antimony isotope fractionation in hydrothermal systems. *Geochimica et*
809 *Cosmochimica Acta*. <https://doi.org/10.1016/j.gca.2021.05.031>
- 810 Zhou, J., Tian, H., Zhu, C., Hao, J., Gao, J., Wang, Y., Xue, Y., Hua, S., Wang, K., 2015.
811 Future trends of global atmospheric antimony emissions from anthropogenic activities

812 until 2050. *Atmospheric Environment* 120, 385–392.
813 <https://doi.org/10.1016/j.atmosenv.2015.09.018>
814 Zhou, W., Zhou, A., Wen, B., Liu, P., Zhu, Z., Finfrock, Z., Zhou, J., 2022. Antimony isotope
815 fractionation during adsorption on aluminum oxides. *Journal of Hazardous Materials*
816 429, 128317. <https://doi.org/10.1016/j.jhazmat.2022.128317>
817
818
819